Applied Thermal Engineering 289 (2026) 129889

Contents lists available at ScienceDirect

Applied Thermal Engineering

journal homepage: www.elsevier.com/locate/apthermeng

Research Paper

Physics-guided genetic algorithm for optimization of multi-jet impingement cooling

Yonghun Kim [a], Haeun Lee [b,c,*], Seokwon Jeong [d], Nana Kang [d,e], Changwoo Han [e], Dongmin Shin [e], Hyoungsoon Lee [a,d,**]

[a] School of Mechanical Engineering, Chung-Ang University, Seoul 06974, Republic of Korea
[b] Department of Mechanical Engineering, Stanford University, Stanford, CA 94305, USA
[c] Department of Automotive Engineering, Yeungnam University, Gyeongsan 38541, Republic of Korea
[d] Department of Intelligent Energy and Industry, Chung-Ang University, Seoul 06974, Republic of Korea
[e] Research & Development Division, Hyundai Motor Group, Hwaseong 18280, Republic of Korea

A R T I C L E I N F O

Keywords:
Multi-jet impingement cooling
Machine learning
Multimodal machine learning
Physics-guided
Genetic algorithm
Thermal management

A B S T R A C T

Efficient thermal management is essential for maximizing the performance and reliability of power semiconductor devices, particularly in data centers, electric vehicles, drive motors, and photovoltaic systems. Multi-jet impingement cooling has emerged as a promising solution, offering enhanced heat transfer from thinning boundary layers, and localized cooling capabilities, but its optimization remains challenging due to the complexity and high dimensionality of the design parameter space. This study develops machine learning framework coupled with a genetic algorithm to efficiently predict and optimize the thermal and hydraulic performance of multi-jet impingement cooling. We trained scalar and multimodal machine learning models using comprehensive computational fluid dynamics simulations, incorporating physical principles to enhance predictive accuracy. As a result, prediction errors decreased substantially, from 408.2% to 10.3% for pressure drop and from 25.9% to 3.7% for maximum temperature. Compared to conventional computational approaches, our proposed methodology significantly reduces computational effort and accelerates the identification of optimal cooling configurations. This study presents a robust and efficient strategy for advancing thermal management solutions critical to next generation high power semiconductor applications.

1. Introduction

Rapid advancements in semiconductor technologies such as wide bandgap (WBG) materials, including silicon carbide (SiC) and gallium nitride (GaN), have significantly increased power densities in electronic devices, exacerbating thermal management challenges. In electric vehicles (EVs), power electronics modules experience elevated heat flux conditions, critically impacting efficiency and reliability if not properly managed [1,2]. Similarly, data centers, driven by heterogeneous integration and advanced three-dimensional chip architectures, suffer from intensified localized heat generation and thermal cross-talk, leading to increased cooling demands [3]. Consequently, thermal management systems in data centers alone account for up to 40% of total energy consumption, highlighting the critical need for efficient cooling solutions capable of maintaining performance and sustainability [4,5].

Various advanced cooling technologies have been explored to address high heat flux conditions, including microchannels [6,7], micropin fins [8,9], manifold microchannel [10,11], spray cooling [12], jet impinging cooling [13,14], nanofluids [15], and electrohydrodynamic (EHD) cooling [16,17]. Among these approaches, Multi-Jet Impingement Cooling (MJIC) has emerged as a highly effective method due to its ability to reduce thermal boundary layers and achieve localized, high-velocity fluid flow, enhancing heat transfer significantly [18]. Previous MJIC studies have primarily focused on the parametric investigation of nozzle geometries and operational conditions, revealing significant dependencies on nozzle arrangements, jet diameters, and jet-to-target distances. Jambunathan et al. [19] analyzed jet diameter and impingement distances for single jets, while Geers et al. [20] demonstrated enhanced heat transfer from complex multi-jet vortex interactions. San

* Corresponding authors at: Department of Mechanical Engineering, Stanford University, Stanford, CA 94305, USA.
** Corresponding authors at: School of Mechanical Engineering, Chung-Ang University, Seoul 06974, Republic of Korea.
E-mail addresses: haeunlee@yu.ac.kr (H. Lee), leeh@cau.ac.kr (H. Lee).
URL: https://atsla.cau.ac.kr (H. Lee).

https://doi.org/10.1016/j.applthermaleng.2026.129889
Received 9 September 2025; Received in revised form 7 December 2025; Accepted 21 January 2026
Available online 25 January 2026

Nomenclature

A	Area (mm^2)
CFD	Computational Fluid Dynamics
CNN	Convolutional Neural Network
d	Jet hole diameter (mm)
D_n	Diameter of the nozzle (mm)
D_{eq}	Equivalent diameter (mm)
EVs	Electric Vehicles
GA	Genetic Algorithm
h	Heat transfer coefficient ($kW \cdot m^{-2} \cdot K^{-1}$)
H	Distance from jet exit to impingement plate (mm)
HTC	Heat Transfer Coefficient ($kW \cdot m^{-2} \cdot K^{-1}$)
k	Thermal conductivity
$\dot{m}$	Mass flow rate ($kg \cdot s^{-1}$)
$MAPE$	Mean Absolute Percentage Error
ML	Machine Learning
MLP	Multi-Layer Perceptron
$MJIC$	Multi-Jet Impingement Cooling
N_n	Number of nozzles (−)
Nu_H	Nusselt number based on nozzle-surface spacing H (−)
$NSGA\text{-}II$	Non-Dominated Sorting Genetic Algorithm
P	Pressure (mbar)
ΔP	Pressure drop (mbar)
P_{pump}	Pumping power (W)
PEC	Performance Evaluation Criterion
q	Heating power (W)
Q	Volume flow rate (LPM)
Re	Reynolds number
s	Jet-to-jet spacing (mm)
SST	Shear Stress Transport
T_{avg}	Average temperature (°C)
T_{in}	Inlet temperature (°C)
T_{max}	Maximum temperature (°C)
T_{heated}	Temperature of heated area (°C)
T_{surf}	Temperature of target surface (°C)
TKE	Turbulent Kinetic Energy ($m^2 \cdot s^{-2}$)
ΔT	Temperature difference (°C)
U_b	Bulk velocity
v	Velocity
$\dot{V}$	Volume flow rate ($m^3 \cdot s^{-1}$)
WBG	Wide Bandgap
$y+$	Dimensionless wall distance (−)

Greek symbols

μ	Dynamic viscosity (Pa•s)
ν	Kinematic viscosity ($m^2 \cdot s^{-1}$)
ρ	Density ($kg \cdot m^{-3}$)

Subscripts

avg	Average
b	Bulk
f	Fluid
heated	Heated area
in	Inlet
max	Maximum
n	Nozzle
out	Outlet
surf	Target surface

and Chen [21] found that maximum Nusselt numbers occur between jets in multi-circular arrays at low inter-nozzle spacing ($s/d = 2.0$) and jet height ($H/d = 0.5$). Tepe et al. [14] indicated that minimizing jet interference through nozzle proximity improves local cooling. Recently, Wei et al. [22] studied nozzle geometry across Reynolds numbers (32–2048), developing predictive correlations. Despite these advancements, practical optimization remains limited by the extensive computational cost of iterative computational fluid dynamics (CFD) simulations and simplified empirical correlations.

Machine learning (ML) has emerged as an efficient alternative to conventional optimization methods by accurately predicting thermal performance with substantially reduced computational cost. Unlike traditional empirical correlations confined to specific operational conditions, ML models can effectively capture intricate relationships among geometric configurations, operating parameters, and resulting thermal behaviors. Several studies have demonstrated the potential of ML for thermal system optimization. Kwon et al. [23] and Kim et al. [24] utilized scalar-based ML algorithms to accurately predict heat transfer coefficients, significantly outperforming conventional correlations. Yesilyurt et al. [25] applied deep neural networks (DNN) to predict hourly building energy consumption and proposed effective energy management strategies. Farhadi et al. [26] employed Extra Trees and LightGBM models to accurately predict the performance of evacuated tube solar collectors, demonstrating the potential for optimizing thermal energy systems. Further advancements by Moon et al. [27], Nguyen et al. [28], and Yang et al. [29] integrated scalar-based ML with genetic algorithms (GA) and hybrid neural network-GA frameworks, enhancing thermal optimization capabilities. However, these scalar-centric approaches inherently neglected spatial temperature distributions, limiting their ability to capture localized heat-transfer phenomena accurately. Recently, Lee et al. [30] attempted to address this limitation by employing multimodal ML approaches integrating spatial image data; however, their methods involved conventional image processing techniques, resulting in relatively high computational costs. Additionally, Lee et al. [31] developed physics-informed XGBoost models that significantly improved predictive accuracy compared to purely data-driven approaches, although still primarily relying on scalar inputs. A more advanced approach, the Physics-Informed Neural Network (PINN) proposed by Raissi et al. [32], integrates governing equations directly into the neural network's loss function to enforce physical laws. However, this method's reliance on explicit physical models becomes a significant limitation for systems with highly complex phenomena or ill-defined governing equations, such as in a MJIC. Consequently, there remains a clear need for a computationally efficient ML framework capable of accurately integrating spatial temperature distributions, enabling effective optimization without the computational complexity of traditional image-processing techniques.

In this study, ML models trained on comprehensive CFD datasets are developed to accurately predict the thermal and hydraulic performance of MJIC systems. Two frameworks are proposed: a scalar-based model utilizing geometric and operational parameters, and a multimodal model integrating spatial temperature distributions with scalar inputs. Unlike conventional scalar-only or computationally intensive image-processing approaches, the multimodal method leverages spatial temperature data to enhance prediction accuracy. Furthermore, these ML models are integrated into a physics-guided GA, employing physics-based constraints to guarantee realistic and computationally efficient optimization results. This integrated framework enables rapid identification of optimal MJIC nozzle configurations, considerably reducing computational effort while enhancing practical applicability for energy-intensive applications, including electric vehicles and data centers.

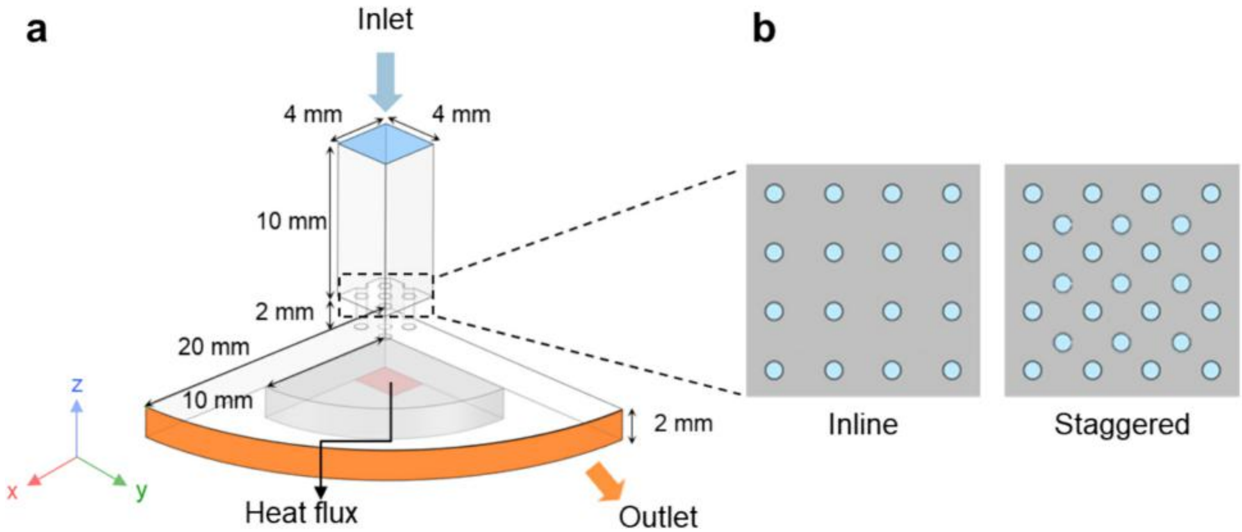

Fig. 1. Simulation model and nozzle configurations. a, Quarter model of the device with boundary conditions. b, Inline and staggered nozzle configurations. To reduce computational cost, the unit cell was analyzed by applying quarter symmetry, using the *xz* and *yz* planes as symmetric boundaries.

Table 1
. Design space definition.

Parameter	Value	Unit
N_n	1, 4, 5, 9, 13, 16, 25, 36, 41, 49, 61, 64, 85, 100, 113, 144, 181, 196, 256, 365	–
D_n	0.2, 0.4, 0.6, 0.8, 1.0	mm
$\dot{m}$	1.5, 2.0, 2.5, 3.0	LPM
Configuration	Inline, Staggered	–

2. Method

2.1. Comprehensive datasets for multi-jet impingement cooling

Comprehensive datasets were generated through systematic CFD simulations to train ML models for accurately predicting and optimizing the thermal-hydraulic performance of MJIC systems. Thermal-hydraulic performance of MJIC significantly depends on geometric parameters, such as nozzle diameter, arrangement, and number, as well as operating conditions including fluid flow rate. Accurate flow analysis is crucial for optimization due to potential interactions between adjacent jets.

2.1.1. CFD-based data generation and simulation setup

Simulations were conducted using a unit cell rather than the entire cooling module to reduce computational costs. As illustrated in Fig. 1a, the unit cell consists of a fluid domain (top) and a solid domain (bottom). The solid domain includes a 6.4×5 mm^2 heat source representing a SiC semiconductor chip and a 2-mm-thick Al1060 aluminum substrate with a 10-mm radius for thermal spreading. Fluid enters through an 8×8 mm^2 inlet, passes through a 10-mm inlet plenum and a 2-mm-long

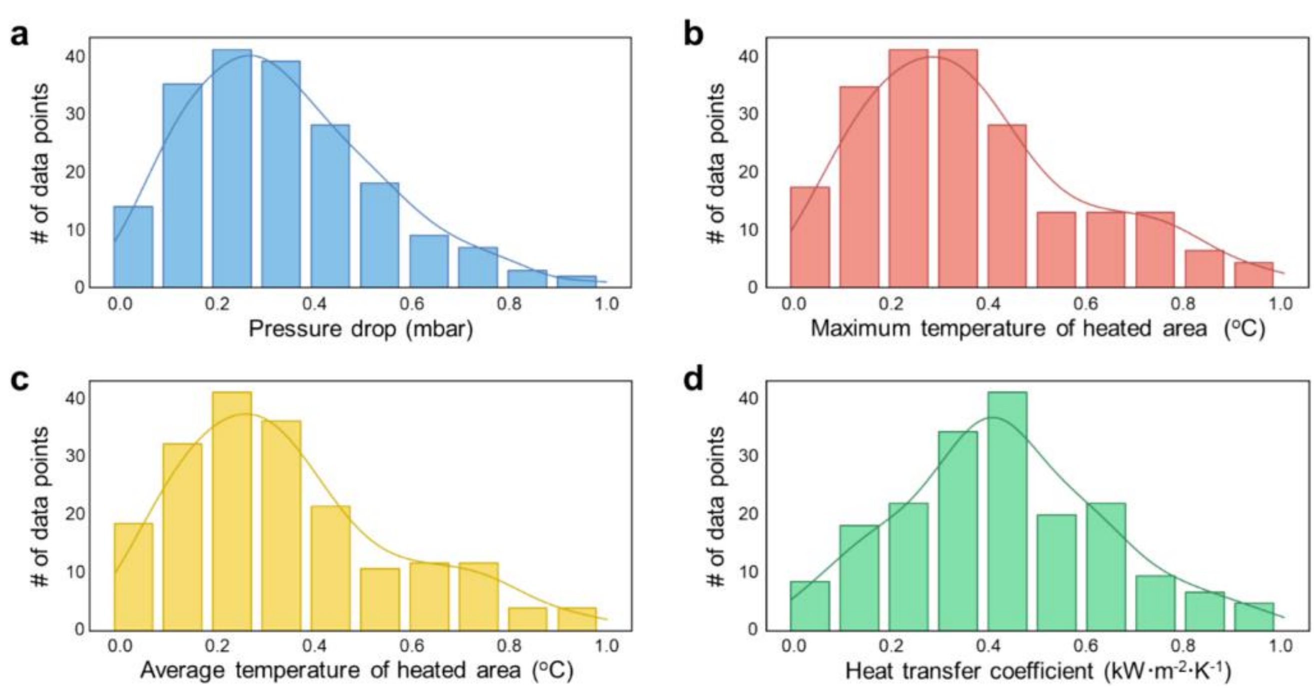

Fig. 2. Statistical distribution of dataset parameters. **a,** Pressure drop. **b,** Maximum temperature. **c,** Average temperature. **d,** Heat transfer coefficient. These metrics were used as output parameters to evaluate cooling performance in the machine learning models.

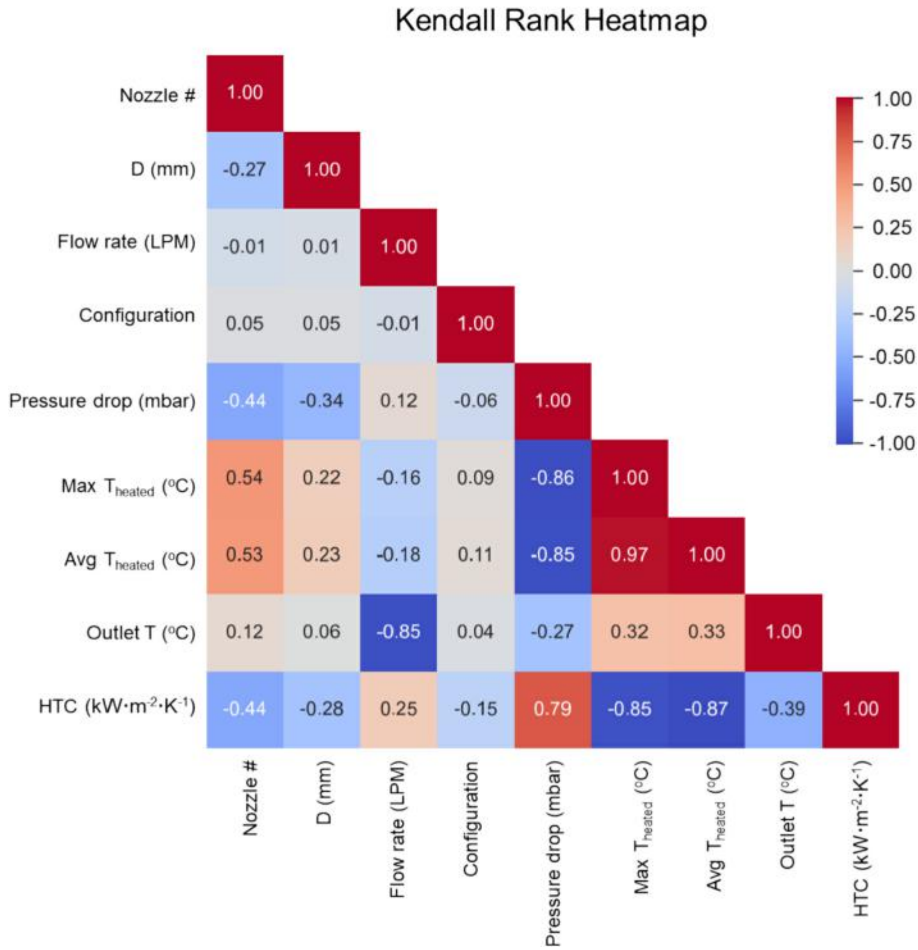

Fig. 3. Kendall rank correlation heatmap of dataset parameters. Key parameters influencing cooling performance were identified. Outlet temperature was excluded from the machine learning analysis because it was strongly correlated only with flow rate, showing independence from nozzle geometry.

nozzle, impinges on the heated surface, and then exits radially outward over a 20-mm radius region. Quarter symmetry was applied along the *xz* and *yz* planes to further minimize computation time.

Two nozzle configurations, inline and staggered as shown in Fig. 1b, were evaluated. The design space included nozzle counts from 1 to 365, nozzle diameters from 0.2 mm to 1.0 mm and volumetric flow rates from 1.5 to 3.0 LPM, as summarized in Table 1. Performance was evaluated using the maximum and area averaged surface temperatures, the heat transfer coefficient (HTC) and the pressure drop. The HTC was computed as the imposed heat flux divided by the temperature difference between the area averaged surface temperature and the inlet temperature. A uniform heat flux of 885.9 $W \cdot cm^{-2}$, corresponding to a total heat input of 283.5 W, was applied to the heat source. Water at 30 °C was used as the coolant and entered the domain at prescribed mass flow rates before exiting at ambient pressure. The coolant was modeled as a single phase fluid without phase change or nanofluid effects. Depending on the nozzle geometry and flow rate, the inlet Reynolds number varied from 3.81×10^2 to 4.03×10^5.

Numerical simulations were performed using ANSYS Fluent 2019 R2. The steady and incompressible conservation equations for mass, momentum and energy were solved in both the fluid and solid regions to account for conjugate heat transfer. The near wall mesh was refined to maintain y^+ values between 5 and 7. Grid independence was confirmed through a five level refinement study. Refining the mesh from 2.443×10^7 cells to the finest mesh changed the maximum temperature by 0.02% and the pressure drop by 0.59%. The full refinement procedure and mesh specifications are provided in Supplementary Note S1 and Table S1.

The k–ω SST turbulence model was selected based on the validation reported by Elliott and Robinson [33] for millimeter scale impinging jet arrays operating in comparable flow ranges. Their experiments showed maximum deviations of 2.6% in junction temperature and 8.2% in pressure drop. Using the same turbulence model and a similar configuration, the present simulations reproduce their measured junction temperature and pressure drop within 4% and 10%.

2.1.2. Data preprocessing and feature extraction for ML

A total of 308 simulation cases were conducted by combining various design variables to generate training data for ML models. Each case provided nine scalar parameters and two spatial image datasets. Scalar data were preferred due to their low dimensionality, ease of interpretation, and computational efficiency. Scalar input parameters included N_n, D_n, $\dot{m}$, nozzle arrangement, pressure drop, maximum temperature, average temperature, outlet temperature, and HTC. Scalar data were normalized using a Min-Max scaler for consistent scaling. Fig. 2 illustrates the distribution of scalar performance metrics. From the 308 datasets, 10% were randomly selected as the test set, with the remaining 90% divided into training and validation sets at a 7:3 ratio. *K*-fold cross-validation ($K = 5$) was applied to improve model robustness [34].

Next, spatial image data were incorporated to include spatial details not captured by scalar data alone. Specifically, spatial data represented temperature contours of the impinging surface and the nozzle configurations. Temperature contour data provided intuitive guidelines by revealing localized hotspots and patterns caused by jet interference, essential for accurate cooling performance predictions. To avoid the high computational cost associated with conventional RGB image

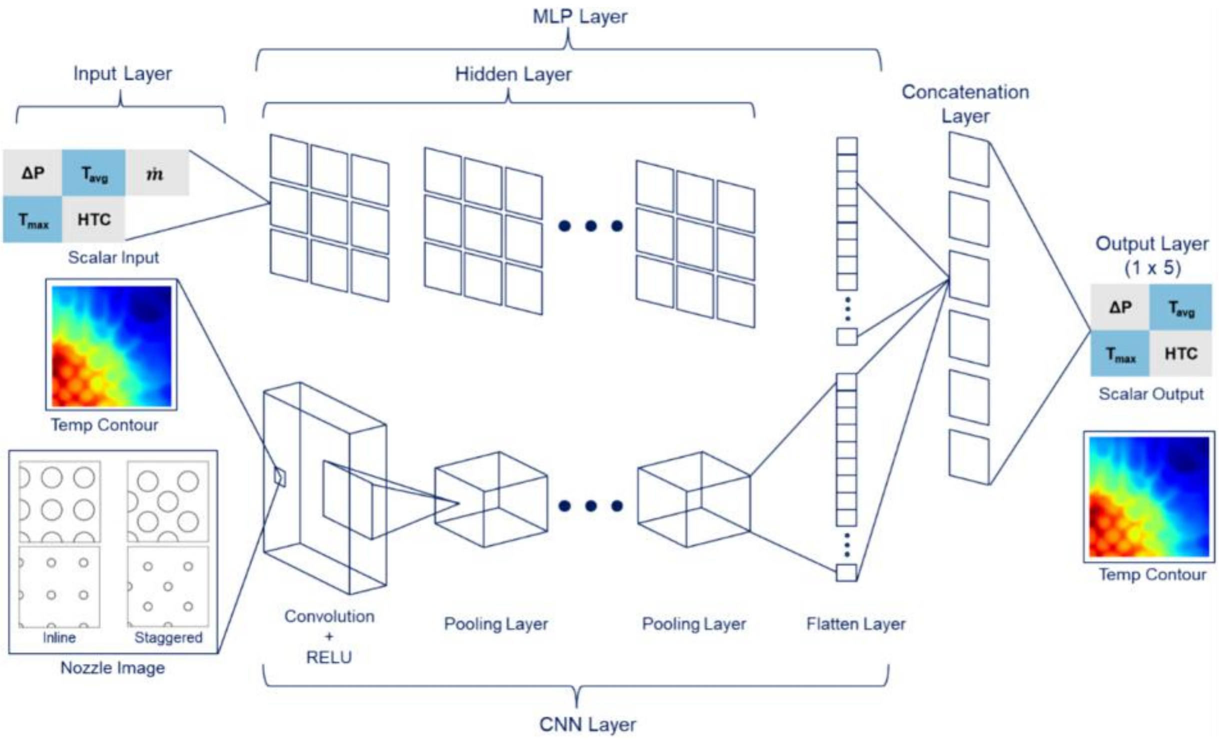

Fig. 4. Multimodal machine learning model architecture. Spatial data (2D) representing temperature distributions and nozzle configurations were integrated with scalar data (1D) including pressure drop, maximum temperature, average temperature, and heat transfer coefficient, in order to enhance predictive accuracy.

processing, the temperature field was extracted directly from the CFD results in the form of numerical matrices with associated physical coordinates. The data were collected over a 5 × 5 mm^2 region that fully covers the nozzle footprint. The field was sampled on a 200 × 200 Cartesian grid (approximately 40,000 points), which preserved the spatial gradients associated with jet interactions. This resampling was performed only to produce fixed-size image inputs for the machine learning models. All quantitative thermal and hydraulic metrics reported in this study were evaluated on the native unstructured mesh.

Nozzle configuration images were generated as binary cross-sectional matrices viewed from the inlet direction, where each nozzle opening was assigned a value of 1 and all other pixels were assigned 0. Because the nozzle layout contains simpler geometric features than the temperature field, lower-resolution images were sufficient. Therefore the nozzle mask was downsampled to 100 × 100 while the temperature contour was retained at 200 × 200 to preserve fine thermal structures. The mask resolution was systematically reduced, and 100 × 100 was identified as the lowest resolution that maintained perimeter and area errors below 1%. This downsampling reduced the training time from 1 h 36 min (200 × 200 resolution) to 49 min (100 × 100 resolution), corresponding to a computational savings of approximately 49%. Even with the reduced mask resolution, the validation R^2 score remained above 0.95.

Prior to ML model training, Kendall rank correlation analyses were performed to identify influential parameters for predicting pressure drop, maximum temperature, average temperature, and *HTC*. Fig. 3 indicates outlet temperature was strongly correlated only with flow rate (−0.85) and independent of nozzle geometry; thus, it represented a simple energy balance and was excluded from subsequent ML analyses. All other parameters with correlation coefficients greater than 0.1 were included to ensure robust and accurate predictions [27].

Initially, ML models were trained solely using scalar data to optimize nozzle configurations. Subsequently, spatial image data were integrated to further enhance predictions by capturing localized temperature distributions and jet-induced hotspots. Finally, optimization results obtained from scalar-based models were systematically compared with those from spatially informed multimodal models to evaluate improvements in prediction accuracy and reliability.

2.2. *Machine learning model development and validation*

ML models were trained using CFD-generated data to accurately predict thermal-hydraulic performance. The developed models were classified into two categories: scalar-based ML, using scalar input parameters, and multimodal ML, which integrates scalar inputs with spatial (2D) image data. All ML models were implemented using Python (version 3.10.0) and TensorFlow (version 2.12.0).

2.2.1. *Scalar-based ML model*

Eight scalar-based ML models were comparatively evaluated to identify the most accurate approach for predicting cooling performance from nozzle configurations. The evaluated models fall into four distinct categories:

Tree-based ensemble models: These algorithms combine multiple decision trees, effectively capturing nonlinear relationships and complex data patterns, thereby enhancing predictive accuracy and generalization. Examples include Decision Tree [35], Random Forest [36], XGBoost [37], and LightGBM [38].

Linear and kernel-based models: These models predict outputs by assuming linearity or leveraging kernel functions to handle nonlinear data. They are computationally efficient and highly interpretable. Representative models include Elastic Net [39], representing linear method, and Support Vector Regression (SVR) [40], a kernel-based method.

Artificial neural network models: These models mimic human neural structures to effectively capture complex nonlinear relationships. A multilayer perceptron (MLP), consisting of interconnected input, hidden, and output layers, was employed. Weights were initialized using He initialization, and the Adam optimizer [41] was applied for training, combining advantages from AdaGrad [42] and RMSprop [43]

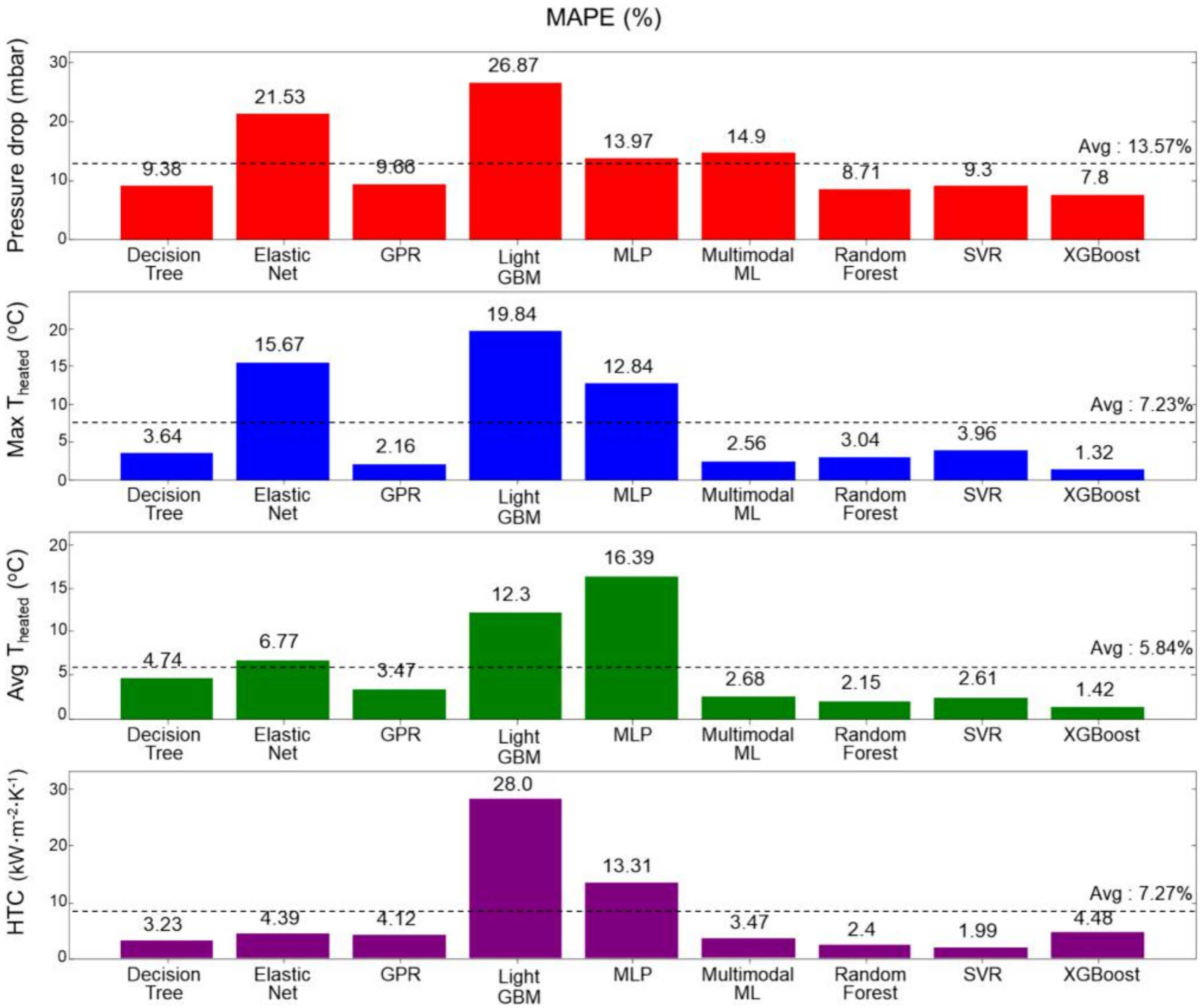

Fig. 5. Comparison of prediction errors across models. Mean absolute percentage errors (MAPE) are presented for four performance metrics: pressure drop, maximum temperature, average temperature, and heat transfer coefficient. Results are shown for scalar-based and multimodal machine learning models evaluated on independent test data.

algorithms.

Probabilistic models: These methods estimate predictions along with their associated uncertainties based on probability distributions. Gaussian Process Regression (GPR) [44], a Bayesian approach defining a prior over functions, was selected for its robustness in small dataset conditions.

2.2.2. Multimodal ML model integration

Multimodal ML techniques were employed to combine scalar and spatial image data, enhancing predictive accuracy through complementary information. Multimodal ML simultaneously processes multiple data types, capturing comprehensive relationships and improving model generalizability [45]. As illustrated in Fig. 4, the multimodal model integrates two distinct data types: spatial (2D) temperature distributions and nozzle configurations, and scalar (1D) data such as pressure drop, maximum temperature, average temperature, HTC, and flow rate.

Spatial features from 2D image data were extracted using a convolutional neural network (CNN), chosen for its effectiveness in capturing complex spatial patterns like localized hotspots and jet interference effects. Concurrently, scalar inputs were processed using an MLP, known for efficiently modeling nonlinear relationships. Features extracted separately from CNN (2D) and MLP (1D) branches were subsequently merged, allowing the multimodal model to leverage correlations between spatial and scalar information. This approach improved prediction performance significantly compared to scalar-only models.

2.3. Optimization framework

2.3.1. Hyperparameter optimization

Bayesian optimization was applied to efficiently determine optimal hyperparameters for all ML models [46]. Hyperparameters were tuned to maximize the 5-fold cross-validation mean R^2 score (R^2) relative to the training dataset. Identical optimization conditions were maintained across all models, ensuring fair comparison, significantly reducing computational resources compared to conventional tuning methods, and minimizing performance variations caused by differences in parameter tuning [47]. In most cases, the search reached stable cross-validated performance within approximately 40 Bayesian-optimization evaluations, where each evaluation corresponds to one 5-fold CV average. The model-specific hyperparameters, search spaces, budgets, and evaluation settings are summarized in Supplementary Note S2 and Table S2.

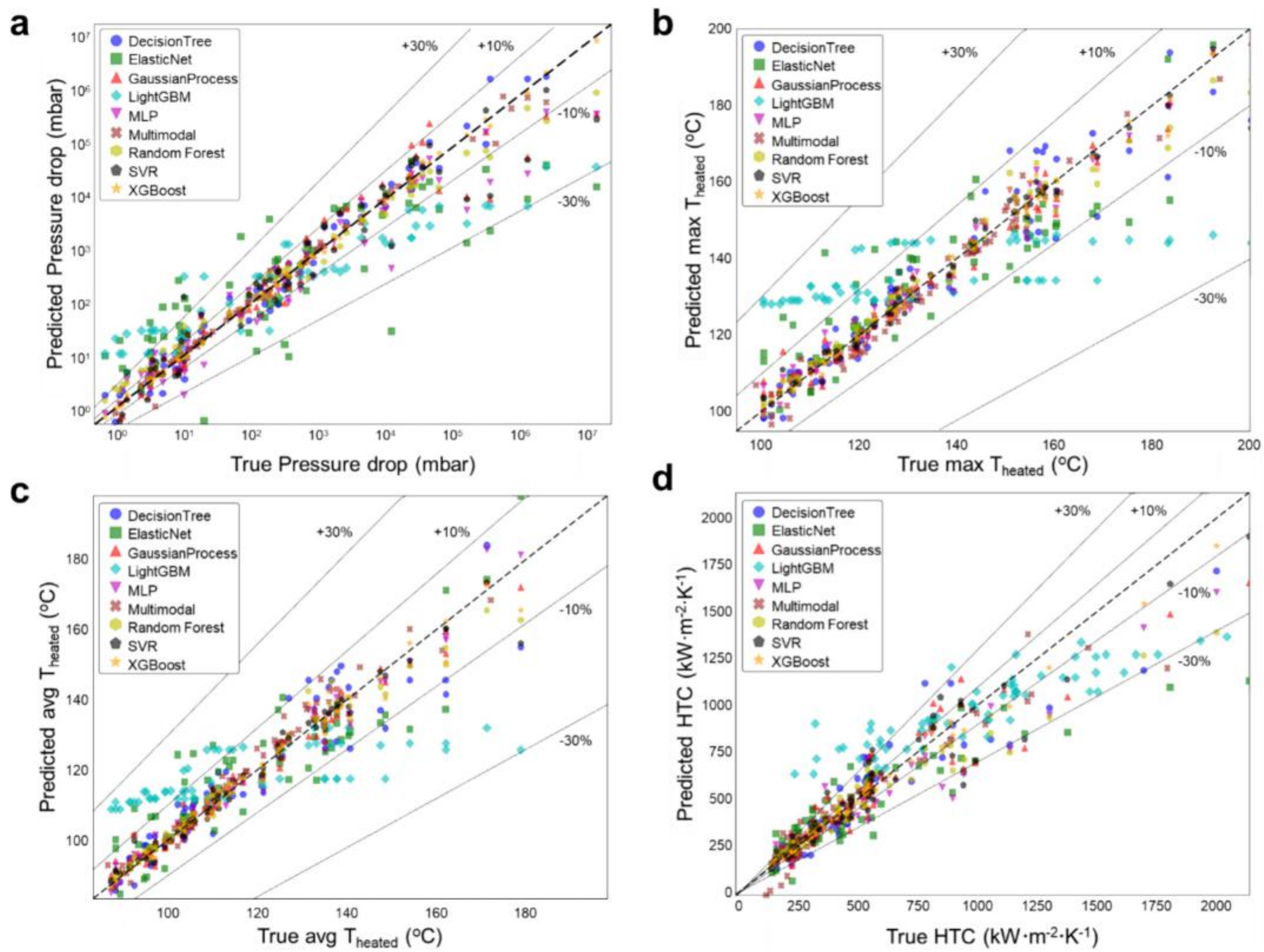

Fig. 6. Evaluation of model predictions against CFD simulations for scalar parameters. Comparison of four performance parameters **a,** Pressure drop. **b,** Maximum temperature. **c,** Average temperature. **d,** Heat transfer coefficient.

2.3.2. *Physics-guided multi-objective optimization*

Multi-objective optimization was conducted using the Non-dominated Sorting Genetic Algorithm II (NSGA-II) [48] to simultaneously minimize maximum temperature and pressure drop, critical metrics for cooling performance. NSGA-II generated Pareto fronts representing optimal trade-offs between competing objectives. Initially, NSGA-II was integrated with the best-performing scalar-based model (XGBoost). Within the defined parameter space, 200 random initial designs were evolved through 100 generations (20,000 evaluations), substantially reducing computational cost (~30 min total) compared to traditional CFD simulations (~4 h per case). Evolutionary steps included crossover (85%), mutation (5%), and unchanged individuals (10%).

Subsequently, NSGA-II was coupled with multimodal ML, incorporating spatial data to permit increased geometric flexibility. However, this flexibility introduced prediction challenges due to deviations from training configurations. To mitigate this, a physics-guided optimization approach was introduced, restricting nozzle configurations to physically realistic patterns similar to training data. A physics-based constraint was enforced as follows (Eq. (1)):

$$P \propto \frac{1}{2} v^2 \text{ where } v = \frac{Q}{A} \tag{1}$$

This physics-guided multimodal framework served two primary purposes: (1) eliminating non-physical solutions violating fundamental fluid-dynamic principles and (2) imposing a penalty within the loss function when predicted pressures deviated significantly (±20% area difference) from CFD-based expectations. This ensured the generation of physically realistic, accurate, and reliable nozzle configurations.

3. Results and discussion

ML models trained on scalar and spatial CFD data were evaluated for predicting and optimizing the thermal-hydraulic performance of multi-jet impingement cooling. The most accurate ML model was integrated with a GA to identify optimal nozzle configurations, which were subsequently validated via CFD simulations. Additionally, a physics-guided multimodal ML framework was developed to ensure physically realistic configurations and further improve prediction accuracy.

3.1. *Performance evaluation of machine learning models*

The accuracy of ML models was evaluated based on four performance metrics: pressure drop, maximum temperature, average temperature, and HTC. Mean Absolute Percentage Error (MAPE) was selected as the evaluation criterion for intuitive representation of relative prediction accuracy across different scales:

$$\text{MAPE } (\%) = \frac{1}{n} \sum_{i=1}^{n} \left| \frac{y_i - \hat{y}_i}{y_i} \right| \times 100 \tag{2}$$

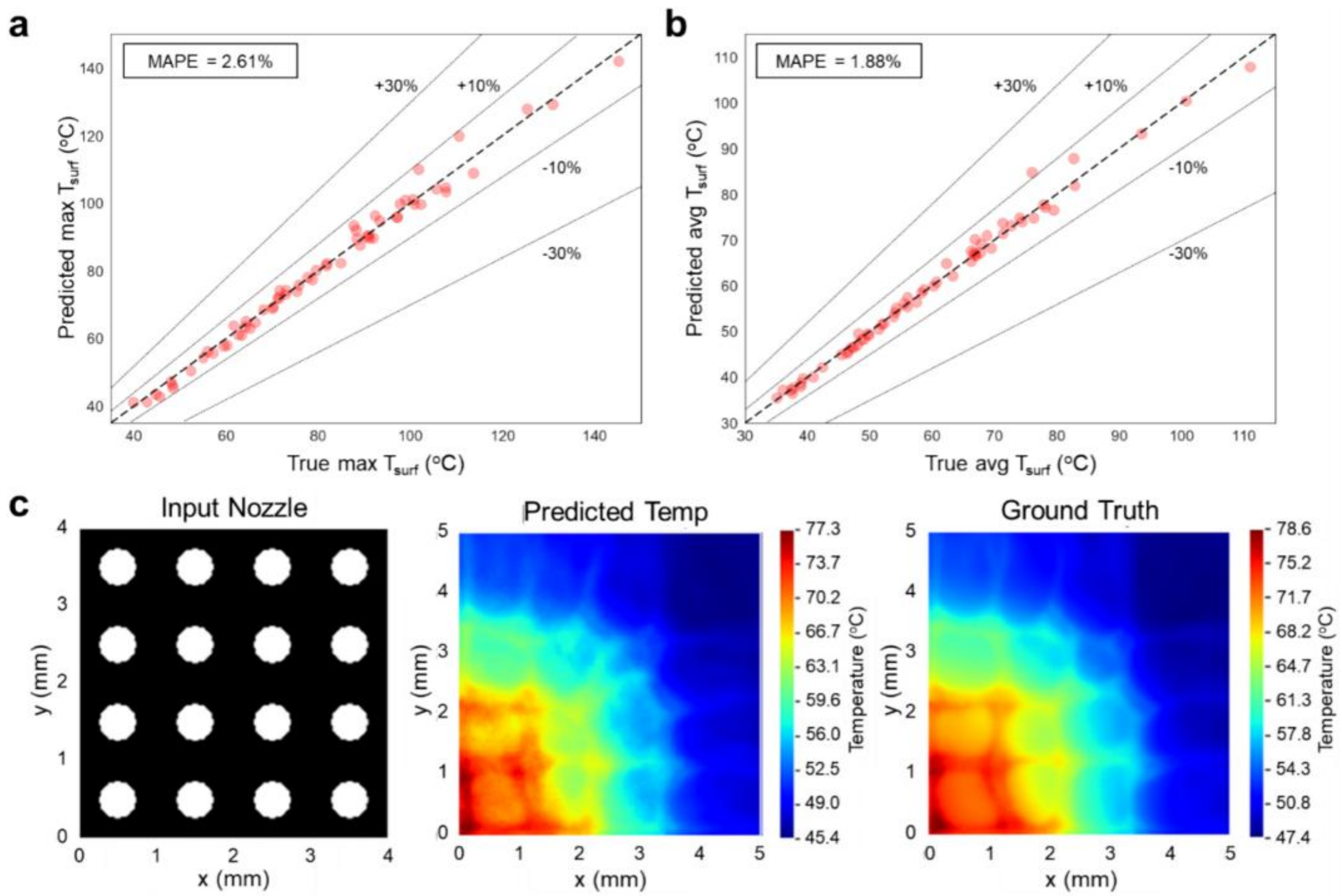

Fig. 7. Validation of the multimodal machine learning model predictions. a, Maximum temperature. **b,** Average temperature. **c,** Spatial temperature distribution. Spatial accuracy was evaluated using a representative case with $N_n = 64$, $D_n = 0.4$ mm, $\dot{m} = 3$ LPM, and an inline configuration from 62 independent test data points.

Fig. 5 summarizes the prediction errors (MAPE) for nine ML models evaluated (eight scalar-based and one multimodal), using 196 training data points and 62 independent test cases. Pressure drop exhibited the highest prediction error (MAPE = 13.57%), reflecting inherent complexity in predicting turbulent flow behavior. In contrast, average temperature predictions had the lowest error (MAPE = 5.84%), indicating reduced sensitivity to localized variations. Intermediate prediction errors were observed for maximum temperature (MAPE = 7.23%) and HTC (MAPE = 8.98%). Among scalar-based models, XGBoost showed notably superior accuracy (pressure drop: 7.8%, maximum temperature: 1.32%), whereas LightGBM exhibited significantly higher errors despite being similarly tree-based. The multimodal ML model, integrating scalar and spatial data, achieved substantially lower MAPEs for maximum temperature (2.56%) and average temperature (2.68%), demonstrating clear performance improvements.

Fig. 6 further investigates the performance differences noted in Fig. 5 by directly comparing detailed ML predictions against CFD simulation results for each parameter: (a) pressure drop, (b) maximum temperature, (c) average temperature, and (d) HTC. The superior performance of XGBoost relative to LightGBM arises from their fundamentally different tree-splitting methods. Specifically, XGBoost employs level-wise tree splitting, creating balanced, generalized tree structures suitable for capturing complex nonlinear patterns in turbulent fluid dynamics and heat transfer phenomena. Conversely, LightGBM employs leaf-wise splitting, which, while computationally efficient, tends to overfit sparse-data regions due to uneven exploration of parameter spaces. Additionally, across all models, prediction accuracy remained high in data-rich regions but deteriorated significantly in sparse-data regions, especially for pressure drop and HTC. The higher errors in sparse-data regions primarily result from limited training data at extreme parameter conditions, restricting models' extrapolation capabilities. Although expanding the dataset would directly resolve this issue, alternative approaches such as error-weighted training, physics-informed constraints, or uncertainty-aware modeling could enhance predictive reliability without extensive additional CFD simulations.

Fig. 7 demonstrates the performance of the multimodal ML model in predicting temperature distributions in a multi-jet impingement cooling system. The multimodal model was evaluated based on scalar temperature metrics (maximum and average temperatures) and spatially resolved full-field temperature contours, highlighting its ability to accurately capture localized thermal variations that scalar-based models inherently neglect. Evaluated using 62 independent test cases, the multimodal ML model achieved significantly low prediction errors, with MAPEs of 2.61% and 1.88% for maximum and average temperatures, respectively (Fig. 7a, b). These results represent a substantial improvement compared to scalar-based models, which exhibit higher errors due to their inability to account for spatial variations in heat dissipation. Fig. 7c further validates the model's spatial prediction capabilities by comparing the predicted temperature contour with CFD-generated reference data for a representative MJIC configuration ($N_n = 64$, $D_n = 0.4$ mm, $\dot{m} = 3$ LPM, inline configuration). The predicted temperature distribution closely matches the CFD reference, successfully capturing localized temperature drops induced by wall jet flows from individual nozzles. These findings clearly demonstrate the multimodal ML model's superior capability in accurately modeling complex, spatially varying thermal behaviors.

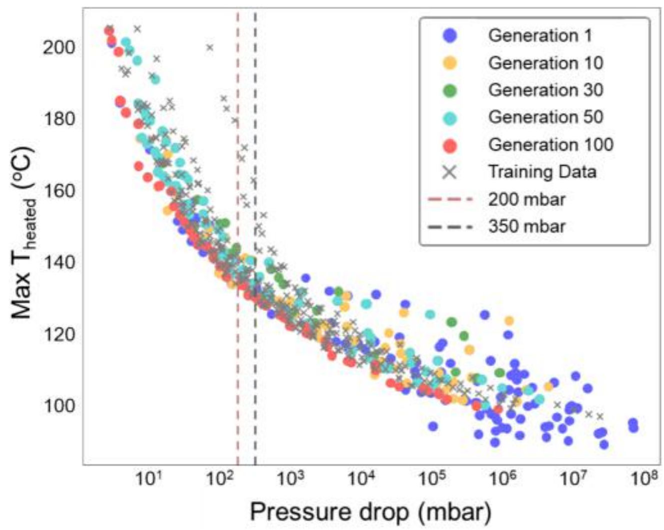

Fig. 8. Pareto front from scalar-based genetic algorithm optimization. Each generation consisted of 200 design points. The final generation (red points) demonstrated average improvements of 11.0% in maximum temperature and 33.1% in pressure drop relative to the initial generation.

3.2. Genetic algorithm-based optimization of nozzle configurations

3.2.1. Scalar-based optimization using genetic algorithm

Fig. 8 illustrates the Pareto front obtained by integrating the scalar-based ML model with a genetic algorithm, clearly visualizing the trade-off between maximum temperature and pressure drop, both essential metrics in evaluating cooling performance. The initial generation, indicated by blue points, directly corresponds to the dataset used for training the scalar-based ML model. Subsequent generations (yellow, green, cyan points) demonstrate progressive evolutionary improvement toward optimal configurations, eventually converging at the final 100th generation (red points). Each generation contains 200 design points, providing comprehensive coverage of the parameter space to ensure robust optimization outcomes. The inverse correlation depicted in Fig. 8 reflects fundamental physical principles underlying MJIC performance. Configurations aiming to reduce maximum temperature generally involve increased fluid velocities and intensified jet impingement effects, which inherently lead to higher pressure drops. Conversely, configurations optimized for lower pressure drops typically result in reduced fluid velocities, thus limiting heat transfer effectiveness and elevating temperatures. Clearly recognizing this intrinsic trade-off emphasizes the practical value of Pareto front analysis, enabling engineers to systematically evaluate conflicting performance objectives and identify practically optimal thermal management solutions.

To validate the practical applicability of these optimized configurations, two representative operating pressures were selected: 200 mbar, reflecting common automotive inverter cooling conditions, and 350 mbar, representing high-performance electric vehicle cooling scenarios. Optimal nozzle configurations minimizing the maximum temperature under each pressure condition were selected from the final Pareto front and rigorously validated through detailed CFD simulations, as summarized in Table 2. The maximum discrepancy between ML predictions and CFD validations was approximately 8.93%, specifically for pressure drop at the 350 mbar condition. This discrepancy primarily stems from inherent limitations of ML models in accurately predicting complex turbulent flow behaviors, particularly under sparse training data conditions. Nevertheless, the optimized configurations demonstrated reliable practical applicability, effectively satisfying targeted thermal and hydraulic performance criteria. Specifically, at 200 mbar, the CFD-validated optimized design achieved a slight improvement in maximum temperature compared to the best-performing training data, from 134.41 °C to 134.2 °C. At 350 mbar, the improvement was more evident, reducing the maximum temperature from 131.22 °C to 131.08 °C. These modest improvements reflect the constraints of the scalar based genetic algorithm, which varies nozzle diameter and flow rate while preserving the overall nozzle arrangement. Since the main flow structures, including boundary layer formation and recirculation behavior, remain similar, the improvements remain incremental. Even so, the consistency of the optimized designs and their agreement with CFD results demonstrate the robustness of the method and its usefulness as a practical guideline for engineering thermal management applications.

3.2.2. Enhanced optimization with physics-guided multimodal ML

To further enhance predictive accuracy and geometric flexibility beyond scalar-based optimization, multimodal ML was integrated with GA. Multimodal ML incorporates spatial temperature distribution data, enabling simultaneous optimization of maximum temperature, pressure drop, and temperature uniformity. Emphasizing temperature uniformity is especially important because localized hotspots significantly affect the reliability and lifespan of electronic components. Initial attempts using purely data-driven multimodal ML allowed GA to explore nozzle configurations far beyond the original training dataset, resulting in irregular and physically unrealistic designs. Consequently, substantial discrepancies were observed during CFD validations, particularly for pressure drop and HTC, severely limiting the practical applicability of these preliminary results (see Fig. S1 and Table S3 in Supporting Information). These discrepancies arise mainly from inherent limitations of purely data-driven multimodal ML, especially its difficulty in accurately extrapolating complex turbulent-driven flow behaviors outside the training data scope. To address these limitations, a physics-guided

Table 2
. CFD validation of GA-optimized nozzle configurations.

a) 200 mbar	Configuration	D_n (mm)	N_n (−)	$\dot{m}$ (LPM)	ΔP (mbar)	$Max\ T_{heated}$ (°C)	$Avg\ T_{heated}$ (°C)	HTC (kW•m^{-2}•K^{-1})
Predicted	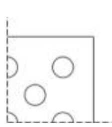	0.96	13	2.77	188.57	136.13	117.20	101.59
CFD					198.41	134.2	116.43	102.5
MAPE		–			4.96%	1.44%	0.66%	0.88%
b) 350 mbar	**Configuration**	**D_n (mm)**	**N_n (−)**	**$\dot{m}$ (LPM)**	**ΔP (mbar)**	**$Max\ T_{heated}$ (°C)**	**$Avg\ T_{heated}$ (°C)**	**HTC (kW•m^{-2}•K^{-1})**
Predicted	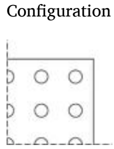	0.67	25	2.81	342.21	132.32	114.56	104.8
CFD					311.65	131.08	113.17	106.5
MAPE		–			8.93%	0.94%	1.21%	1.64%

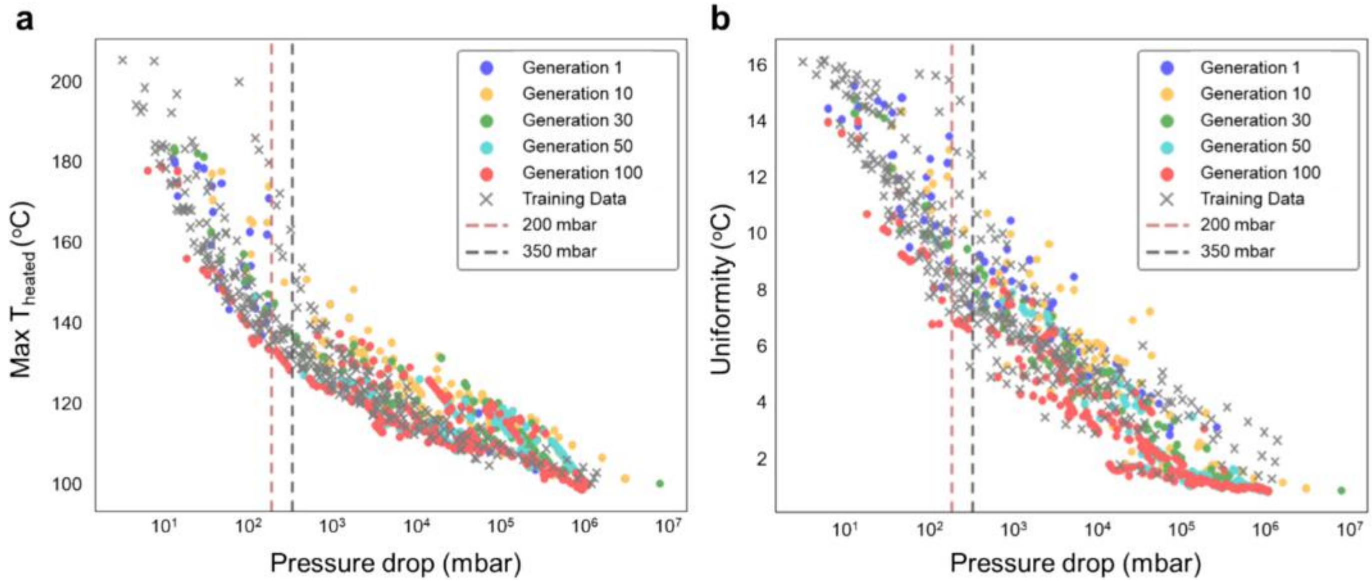

Fig. 9. Pareto fronts generated by physics-guided multimodal machine learning. a, Maximum temperature versus pressure drop. **b,** Temperature uniformity versus pressure drop.

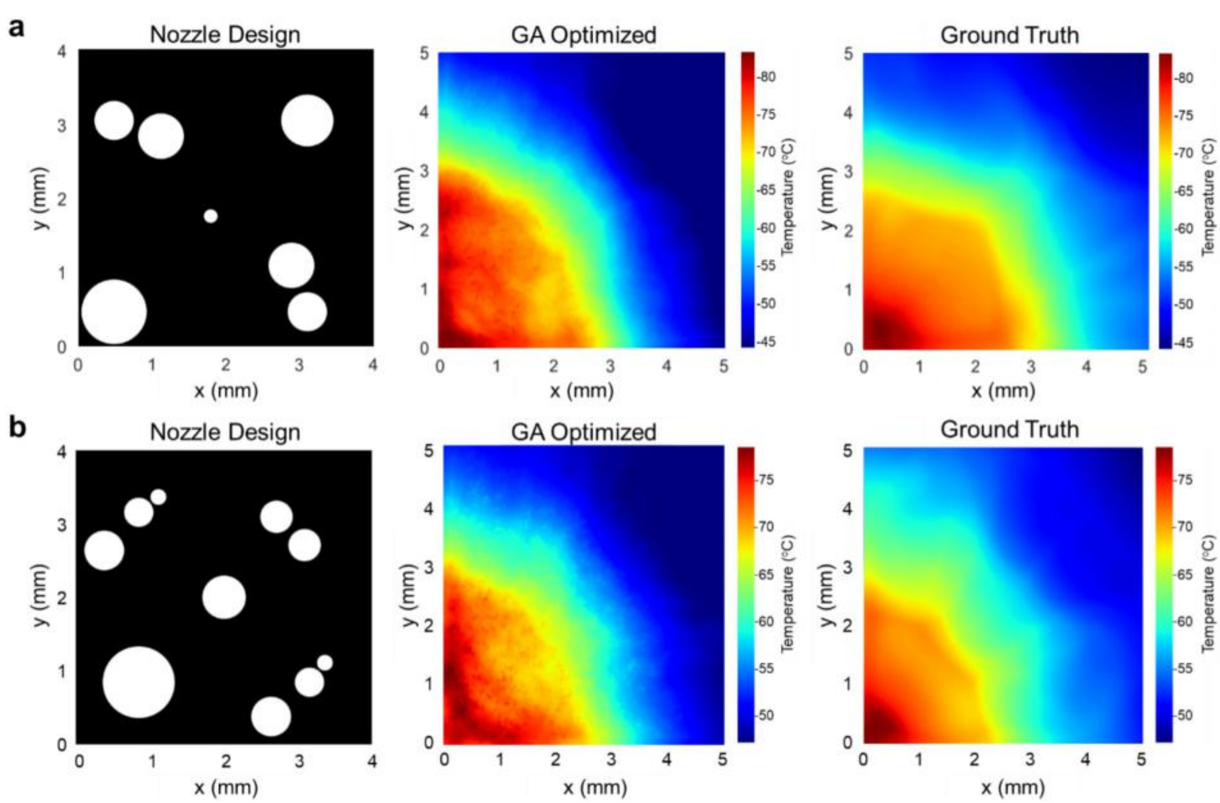

Fig. 10. CFD validation of physics-guided multimodal machine learning nozzle designs. a, Operating condition at 200 mbar. **b,** Operating condition at 350 mbar.

optimization framework was implemented. This approach restricts GA exploration to nozzle layouts consistent with physically feasible fluid-dynamic principles (Eq. 1), thereby significantly improving the multimodal ML-based optimization's predictive accuracy. Fig. 9 presents the Pareto front generated by the physics-guided multimodal ML integrated with GA, clearly demonstrating improved optimization results.

Fig. 10a and b show the optimized nozzle designs and their predicted results using the physics-enhanced multimodal ML with GA. Detailed CFD validation results and associated errors are summarized in Table 3. Incorporating physics-based constraints notably improved prediction accuracy, especially for pressure drop estimations. Compared to the best-performing design from the training dataset, the optimized design at 200 mbar showed a maximum temperature improvement from 134.41 °C to 134.02 °C, although temperature uniformity slightly increased from 9.06 °C to 9.99 °C. At 350 mbar, the optimized design further reduced the maximum temperature from 131.22 °C to 130.27 °C,

Table 3
. CFD validation of physics-guided multimodal GA nozzle configurations.

a) 200 mbar	$\dot{m}$ (LPM)	ΔP (mbar)	Max T_{surf} (°C)	Avg T_{surf} (°C)	Max T_{heated} (°C)	Avg T_{heated} (°C)	HTC (kW•m^{-2}•K^{-1})	Std (°C)
Predicted	2.9	198.77	80.47	56.75	131.91	114.94	101.9	7.88
CFD		199.29	82.81	60.4	134.02	116.16	102.82	9.16
MAPE		0.26%	2.62%	6.43%	1.59%	1.06%	0.91%	16.24%
b) 350 mbar	$\dot{m}$ (LPM)	ΔP (mbar)	Max T_{surf} (°C)	Avg T_{surf} (°C)	Max T_{heated} (°C)	Avg T_{heated} (°C)	HTC (kW•m^{-2}•K^{-1})	Std (°C)
Predicted	2.88	327.66	76.46	55.89	128.39	110.07	110.65	7.31
CFD		343.48	78.6	59.3	130.42	113.15	106.55	7.79
MAPE		4.61%	2.72%	5.75%	1.56%	2.72%	3.84%	6.16%

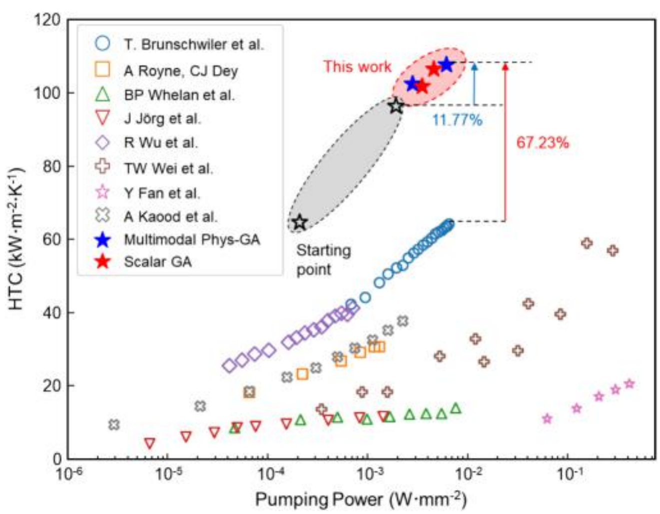

Fig. 11. Benchmark comparison of optimized nozzle designs from relevant studies. The results from previous nozzle jet cooling studies [49–56] are plotted against the normalized pumping power P_{pump}/A_{cool} (W•mm^{-2}). The optimized design in this work achieved a heat transfer coefficient of 107.76 kW·m^{-2}·K^{-1}, which is approximately 67.23% higher than the best previously reported value of 64.24 kW·m^{-2}·K^{-1} from Brunschwiler et al. [49] .

while temperature uniformity improved from 8.10 °C to 7.79 °C. These improvements arise from systematic differences in the flow structures produced by the physics guided layouts. The optimized designs shift regions of high near wall velocity and elevated turbulent kinetic energy into the heated area, registering a 76.1% increase relative to the scalar based baseline. They maintain a more continuous wall jet and weaken fountain type recirculation between nozzles, which thins the local thermal boundary layer and reduces the accumulation of warm fluid above the chip. These effects are illustrated by the turbulent kinetic energy and velocity fields shown in Supplementary Note S5. The predicted temperature contours also align more closely with the CFD fields, capturing the location of local hotspots and the sharp thermal gradients between adjacent jets. These outcomes confirm that integrating physics-based constraints enhances multimodal ML's capability to accurately capture fluid flow behavior and temperature distributions, significantly improving its reliability and practical applicability for engineering thermal management solutions. The dimensionless *Nu* versus *Re* and *ΔP* versus *Re* characteristics for representative layouts are summarized in Supplementary Note S6. A complementary evaluation using the performance evaluation criterion (PEC) is provided in Supplementary Note S7.

3.3. Benchmarking against previous cooling solutions

To evaluate the practical applicability and effectiveness of the proposed optimization approach, a comparative analysis was conducted against previous nozzle-jet cooling studies [49–56] under equivalent operating conditions (i.e., water as working fluid with nozzle-jet impingement). Optimized nozzle designs were compared based on pumping power and *HTC*, as presented in Fig. 11. Here, *HTC* was calculated using Eq. (3):

$$HTC = \frac{q}{A\cdot(T_{avg} - T_{in})} \quad (3)$$

where q is the heating power, A is the heated surface area, T_{avg} is the average temperature of the heated surface, and T_{in} is the inlet temperature. Pumping power was calculated consistently across studies using Eq. (4):

$$P_{pump} = \dot{V} \times \Delta P \quad (4)$$

where ΔP is the pressure drop and V is the volumetric flow rate. The specific design variables and parameter ranges for the comparative analysis are summarized in Table 4.

Among previous studies, Brunschwiler et al. [49] achieved the highest thermal performance using a hierarchical manifold design inspired by biological fluid transport networks such as human blood vessels or tree roots. Their manifold included 19,044 microscopic nozzles arranged in a dense, interconnected inlet and outlet layout, ensuring uniform jet flow distribution and effectively removing a high heat flux of 420 W·cm^{-2}. Although their design demonstrated excellent performance at a given pumping power by optimizing nozzle density and arrangement, the analysis remained limited to regular geometric patterns. In contrast, our optimization approach leverages a genetic

Table 4
. Design variables and performance metrics from previous nozzle-jet cooling studies.

Author/Year	Working fluid	Volume flow rate (LPM)	Number of jet nozzle	Nozzle diameter (mm)	Heated area (cm^2)	Power (W)	Heat transfer coefficient (kW•m^{-2}•K^{-1})	Pumping power (W)
T. Brunschwiler et al. [50]	water	1.17–3.2	19,044	0.043	4	1480	42.28–64.24	0.27–2.58
A Royne, CJ Dey [51]	water	11.5–28.4	4	1.4	7.25	–	18.24–30.78	0.047–0.95
BP Whelan et al. [52]	water	1.97–10	49	1	8.24	100	8.6–13.97	0.038–6.25
J Jörg et al. [53]	water	0.01–0.1	1	0.6	0.4	51	4.27–11.68	0.0002–0.056
R Wu et al. [54]	water	0.8–2.1	44	0.424	5	300–500	25.5–41.3	0.04–0.69
TW Wei et al. [55]	water	0.2–1	16	0.6	0.64	50	18.35–59.07	0.056–9.92
Y Fan et al. [56]	water	0.14–0.31	5	0.4	4	100–400	8.85–20.61	25.0–165.3
A Kaood et al.[57]	water	0.2–2.1	11	1	6.25	625	9.37–37.83	0.0018–1.4

algorithm, enabling exploration and evaluation of arbitrary, irregular nozzle geometries beyond conventional human-driven designs. At a pumping power comparable to that used by Brunschwiler et al. [49], our optimized design achieved an *HTC* of 107.76 $kW\cdot m^{-2}\cdot K^{-1}$, representing an approximate 67.23% improvement over the previously reported value of 64.24 $kW\cdot m^{-2}\cdot K^{-1}$. This substantial improvement highlights the effectiveness of combining multimodal ML with physics-guided GA for thermal optimization, demonstrating superior performance compared to state-of-the-art nozzle-jet cooling strategies.

Overall, this study presents a novel optimization framework for MJIC utilizing spatial image data and physics-guided genetic algorithms, significantly reducing the analysis cost and enabling practical exploration of complex, non-standard geometries. Future studies incorporating more rigorous physical models or direct integration with PDE-based approaches could further enhance the accuracy, reliability, and cost-effectiveness of thermal optimization for high-power electronic systems.

4. Conclusion

This study developed an integrated optimization framework combining machine learning and a physics-guided genetic algorithm to effectively enhance the thermal-hydraulic performance of MJIC systems. The proposed approach significantly reduced computational complexity compared to conventional iterative methods, while ensuring physically realistic and reliable optimization outcomes. Among the scalar-based models evaluated, XGBoost consistently delivered superior predictive accuracy, effectively capturing complex nonlinear thermal-hydraulic behaviors. Incorporating spatial temperature distributions through multimodal ML further enhanced prediction accuracy, reducing mean absolute percentage errors to 2.56% for maximum temperature and 2.68% for average temperature. The introduction of physics-based constraints in the multimodal ML framework effectively addressed previous challenges with unrealistic nozzle configurations, significantly decreasing pressure drop prediction errors from over 400% to below 6.21%, thus markedly improving practical applicability. Optimized nozzle designs obtained via NSGA-II demonstrated substantial performance improvements under realistic operating conditions (200 and 350 mbar), validated by comprehensive CFD analyses. Comparative benchmarking further highlighted the superior performance of the proposed genetic algorithm-driven optimization, achieving approximately 67.23% higher *HTC* compared to previously reported nozzle-jet cooling methods (64.24 $kW\cdot m^{-2}\cdot K^{-1}$ increased to 107.76 $kW\cdot m^{-2}\cdot K^{-1}$).

Collectively, these results underscore the effectiveness of integrating multimodal ML with physics-guided optimization for advancing thermal management solutions in next-generation high-power electronics. Future work should consider enhanced physical modeling, rigorous uncertainty quantification, and adaptive real-time optimization approaches to further improve predictive reliability and practical efficiency.

CRediT authorship contribution statement

Yonghun Kim: Writing – original draft, Methodology, Investigation, Formal analysis, Data curation. **Haeun Lee:** Writing – original draft, Supervision, Methodology, Formal analysis, Data curation. **Seokwon Jeong:** Methodology, Investigation, Formal analysis. **Nana Kang:** Formal analysis, Data curation. **Changwoo Han:** Writing – review & editing, Supervision, Project administration. **Dongmin Shin:** Supervision, Project administration, Funding acquisition. **Hyoungsoon Lee:** Writing – review & editing, Supervision, Project administration, Funding acquisition.

Declaration of competing interest

The authors declare that they have no known competing financial interests or personal relationships that could have appeared to influence the work reported in this paper.

Acknowledgments

This work was supported by the Hyundai Motor Company, the National Research Foundation of Korea(NRF) grant funded by the Korea government(MSIT) (No. RS-2024-00353227), and the Chung-Ang University Graduate Research Scholarship in 2025.

Appendix A. Supplementary data

Supplementary data to this article can be found online at https://doi.org/10.1016/j.applthermaleng.2026.129889.

Data availability

Data will be made available on request.

References

[1] A.F. Pinkos, Y. Guo, Automotive design challenges for wide-band-gap devices used in high temperature capable, scalable power vehicle electronics, in: In *2013 IEEE Energytech*, IEEE, 2013, pp. 1–5.
[2] F.M. Shah, H.M. Xiao, R. Li, M. Awais, G. Zhou, G.T. Bitew, Comparative performance evaluation of temperature dependent characteristics and power converter using GaN, SiC and Si power devices, in: In *2018 IEEE 12th International Conference on Compatibility, Power Electronics and Power Engineering (CPE-POWERENG 2018)*, IEEE, 2018, pp. 1–7.
[3] Q. Zhang, Z. Meng, X. Hong, Y. Zhan, J. Liu, J. Dong, M.J. Deen, A survey on data center cooling systems: technology, power consumption modeling and control strategy optimization, J Syst Archit 119 (2021) 102253.
[4] A.H. Khalaj, S.K. Halgamuge, A review on efficient thermal management of air-and liquid-cooled data centers: from chip to the cooling system, Appl. Energy 205 (2017) 1165–1188.
[5] S. Jones-Jackson, R. Rodriguez, Y. Yang, L. Lopera, A. Emadi, Overview of current thermal Management of Automotive Power Electronics for traction purposes and future directions, IEEE Transactions on Transportation Electrification 8 (2) (2022) 2412–2428, https://doi.org/10.1109/TTE.2022.3147976.
[6] A.M. Sahar, J. Wissink, M.M. Mahmoud, T.G. Karayiannis, M.S.A. Ishak, Effect of hydraulic diameter and aspect ratio on single phase flow and heat transfer in a rectangular microchannel, Appl. Therm. Eng. 115 (2017) 793–814.
[7] H. Zhou, J. Lee, M. Kang, H. Kim, H. Lee, J.B. In, All laser-based fabrication of microchannel heat sink, Mater. Des. 221 (2022) 110968.
[8] C.R. Kharangate, K. Wook Jung, S. Jung, D. Kong, J. Schaadt, M. Iyengar, K. E. Goodson, Experimental investigation of embedded micropin-fins for single-phase heat transfer and pressure drop, J. Electron. Packag. 140 (2) (2018) 021001.
[9] D. Jung, H. Lee, D. Kong, E. Cho, K.W. Jung, C.R. Kharangate, H. Lee, Thermal design and management of micro-pin fin heat sinks for energy-efficient three-dimensional stacked integrated circuits, Int. J. Heat Mass Transfer 175 (2021) 121192.
[10] R. Van Erp, R. Soleimanzadeh, L. Nela, G. Kampitsis, E. Matioli, Co-designing electronics with microfluidics for more sustainable cooling, Nature 585 (7824) (2020) 211–216.
[11] D. Kong, H. Kwon, B. Jang, H.J. Kwon, M. Asheghi, K.E. Goodson, H. Lee, Extreme heat flux cooling from functional copper inverse opal-coated manifold microchannels, Energ. Conver. Manage. 315 (2024) 118809.
[12] N. Zhou, F. Chen, Y. Cao, M. Chen, Y. Wang, Experimental investigation on the performance of a water spray cooling system, Appl. Therm. Eng. 112 (2017) 1117–1128.
[13] H.M. Bahaidarah, Experimental performance evaluation and modeling of jet impingement cooling for thermal management of photovoltaics, Sol. Energy 135 (2016) 605–617.
[14] A.Ü. Tepe, Y. Yetişken, Ü. Uysal, K. Arslan, Experimental and numerical investigation of jet impingement cooling using extended jet holes, International Journal of Heat and Mass Transfer 158 (2020) 119945.
[15] M. Bahiraei, S. Heshmatian, Optimizing energy efficiency of a specific liquid block operated with nanofluids for utilization in electronics cooling: a decision-making based approach, Energ. Conver. Manage. 154 (2017) 180–190.
[16] Y. Kim, S. Jung, S. Kim, S.T. Choi, M. Kim, H. Lee, Heat transfer performance of water-based electrospray cooling, International Communications in Heat and Mass Transfer 118 (2020) 104861.
[17] R.D. Selvakumar, H. Lee, Thermal boundary layer depletion in minichannels by electrohydrodynamic conduction pumping, Appl. Therm. Eng. 230 (2023) 120758.
[18] S.V. Ekkad, P. Singh, A modern review on jet impingement heat transfer methods, J. Heat Transfer 143 (6) (2021) 064001.
[19] K. Jambunathan, E. Lai, M. Moss, B.L. Button, A review of heat transfer data for single circular jet impingement, Int. J. Heat Fluid Flow 13 (2) (1992) 106–115.
[20] L.F. Geers, M.J. Tummers, K. Hanjalić, Experimental investigation of impinging jet arrays, Exp. Fluids 36 (2004) 946–958.

[21] J.Y. San, J.J. Chen, Effects of jet-to-jet spacing and jet height on heat transfer characteristics of an impinging jet array, International Journal of Heat and Mass Transfer 71 (2014) 8–17.
[22] T. Wei, H. Oprins, L. Fang, V. Cherman, E. Beyne, M. Baelmans, Heat transfer and pressure drop correlations for direct on-chip microscale jet impingement cooling with alternating feeding and draining jets, International Journal of Heat and Mass Transfer 182 (2022) 121865.
[23] B. Kwon, F. Ejaz, L.K. Hwang, Machine learning for heat transfer correlations, International Communications in Heat and Mass Transfer 116 (2020) 104694.
[24] K. Kim, H. Lee, M. Kang, G. Lee, K. Jung, C.R. Kharangate, H. Lee, A machine learning approach for predicting heat transfer characteristics in micro-pin fin heat sinks, International Journal of Heat and Mass Transfer 194 (2022) 123087.
[25] H. Yesilyurt, Y. Dokuz, A.S. Dokuz, Data-driven energy consumption prediction of a university office building using machine learning algorithms, Energy 310 (2024) 133242.
[26] S. Farhadi, H.A. Seresht, H. Aghakhani, B. Baghapour, Performance prediction of heat pipe evacuated tube solar collectors: analytical modeling and data-driven machine learning/ANN approach with developing web application, Energy 321 (2025) 135512.
[27] H. Moon, D.J. McGregor, N. Miljkovic, W.P. King, Ultra-power-dense heat exchanger development through genetic algorithm design and additive manufacturing, Joule 5 (11) (2021) 3045–3056.
[28] N.P. Nguyen, E. Maghsoudi, S.N. Roberts, B. Kwon, Shape optimization of pin fin array in a cooling channel using genetic algorithm and machine learning, International Journal of Heat and Mass Transfer 202 (2023) 123769.
[29] J. Yang, K. Cheng, K. Zhang, C. Huang, X. Huai, Hybrid artificial neural networks-based approaches predicting the heat transfer and flow characteristics of manifold microchannels, Appl. Therm. Eng. 257 (2024) 124446.
[30] H. Lee, G. Lee, K. Kim, D. Kong, H. Lee, Multimodal machine learning for predicting heat transfer characteristics in micro-pin fin heat sinks, Case Stud. Therm. Eng. 57 (2024) 104331.
[31] H. Lee, C. Lee, H. Lee, Physics-informed machine learning for enhanced prediction of condensation heat transfer, Energy AI 20 (2025) 100482.
[32] M. Raissi, P. Perdikaris, G.E. Karniadakis, Physics-informed neural networks: a deep learning framework for solving forward and inverse problems involving nonlinear partial differential equations, J. Comput. Phys. 378 (2019) 686–707.
[33] J.W. Elliott, A.J. Robinson, Optimized liquid impinging jet arrays for cooling CPU packages, IEEE Trans. Compon. Packag. Manuf. Technol. 15 (3) (2024) 488–505.
[34] T. Fushiki, Estimation of prediction error by using K-fold cross-validation, Stat. Comput. 21 (2011) 137–146.
[35] J. Ross. Quinlan, Induction of decision trees, Machine learning 1 (1) (1986) 81–106.
[36] L. Breiman, Random forests, Machine learning 45 (1) (2001) 5–32.
[37] Chen, T., & Guestrin, C. (2016). "XGBoost: a scalable tree boosting system". Proceedings of the 22nd ACM SIGKDD international conference on knowledge discovery and data mining.
[38] G. Ke, et al., LightGBM: A Highly Efficient Gradient Boosting Decision Tree, 2017 (Advances in Neural Information Processing Systems).
[39] H. Zou, T. Hastie, Regularization and variable selection via the elastic net, J. R. Stat. Soc. Series B Stat. Methodology 67 (2) (2005) 301–320.
[40] H. Drucker, C.J. Burges, L. Kaufman, A. Smola, V. Vapnik, Support vector regression machines, Advances in neural information processing systems 9 (1996).
[41] Kingma, D. P. (2014). Adam: a method for stochastic optimization. *arXiv preprint arXiv:1412.6980*.
[42] J.C. Duchi, P.L. Bartlett, M.J. Wainwright, Randomized Smoothing for (Parallel) Stochastic Optimization, in: 2012 IEEE 51st IEEE Conference on Decision and Control (CDC), Maui, HI, USA, 2012, pp. 5442–5444, https://doi.org/10.1109/CDC.2012.6426698.
[43] T. Tieleman, G. Hinton, Lecture 6.5-Rmsprop, Coursera: Neural Networks for Machine Learning, University of Toronto, 2012 *(Technical Report, 6.)*.
[44] C. Williams, C. Rasmussen, Gaussian processes for regression, Advances in neural information processing systems 8 (1995).
[45] Ma, L., Lu, Z., Shang, L., & Li, H. (2015). Multimodal convolutional neural networks for matching image and sentence. In *proceedings of the IEEE international conference on computer vision* (pp. 2623-2631).
[46] J. Snoek, H. Larochelle, R.P. Adams, Practical bayesian optimization of machine learning algorithms, Adv. Neural Inf. Proces. Syst. 25 (2012).
[47] R. Turner, D. Eriksson, M. McCourt, J. Kiili, E. Laaksonen, Z. Xu, I. Guyon, Bayesian optimization is superior to random search for machine learning hyperparameter tuning: Analysis of the black-box optimization challenge 2020, in: NeurIPS 2020 Competition and Demonstration Track, PMLR, 2021, pp. 3–26.
[48] K. Deb, A. Pratap, S. Agarwal, T.A.M.T. Meyarivan, A fast and elitist multiobjective genetic algorithm: NSGA-II, IEEE Trans. Evol. Comput. 6 (2) (2002) 182–197.
[49] T. Brunschwiler, H. Rothuizen, M. Fabbri, U. Kloter, B. Michel, R.J. Bezama, G. Natarajan, Direct liquid jet-impingment cooling with micron-sized nozzle array and distributed return architecture, in: Thermal and Thermomechanical Proceedings 10th Intersociety Conference on Phenomena in Electronics Systems, 2006. ITHERM 2006, IEEE, 2006, May, pp. 196–203.
[50] A. Royne, C.J. Dey, Effect of nozzle geometry on pressure drop and heat transfer in submerged jet arrays, International Journal of Heat and Mass Transfer 49 (3–4) (2006) 800–804.
[51] B.P. Whelan, R. Kempers, A.J. Robinson, A liquid-based system for CPU cooling implementing a jet array impingement waterblock and a tube array remote heat exchanger, Appl. Therm. Eng. 39 (2012) 86–94.
[52] J. Jörg, S. Taraborrelli, G. Sarriegui, R.W. De Doncker, R. Kneer, W. Rohlfs, Direct single impinging jet cooling of a MOSFET power electronic module, IEEE Trans. Power Electron. 33 (5) (2017) 4224–4237.
[53] R. Wu, Y. Fan, T. Hong, H. Zou, R. Hu, X. Luo, An immersed jet array impingement cooling device with distributed returns for direct body liquid cooling of high power electronics, Appl. Therm. Eng. 162 (2019) 114259.
[54] T.W. Wei, H. Oprins, V. Cherman, E. Beyne, M. Baelmans, Experimental and numerical investigation of direct liquid jet impinging cooling using 3D printed manifolds on lidded and lidless packages for 2.5 D integrated systems, Appl. Therm. Eng. 164 (2020) 114535.
[55] Y. Fan, X. Zhang, L. Xiang, Y. Cheng, X. Luo, A compact jet array impingement cooling system driven by integrated piezoelectric micropump, Int. J. Heat Mass Transf. 205 (2023) 123905.
[56] A. Kaood, I.O. Elhagali, M.A. Hassan, Investigation of high-efficiency compact jet impingement cooling modules for high-power applications, Int. J. Therm. Sci. 184 (2023) 108006.